

Re-analysis of Temperature Dependent Neutron Capture Rates and Stellar β^- decay Rates of $^{95-98}\text{Mo}$.

Abdul Kabir¹, Jameel-Un Nabi², Muhammad Tahir², Abdul Muneem³ and Zain Ul Abideen¹.

¹Space and Astrophysics Research lab, National Centre of GIS and Space Applications, Department of Space Science, Institute of Space Technology, Islamabad 44000, Pakistan.

²University of Wah, Quaid Avenue, Wah Cantt 47040, Punjab, Pakistan.

³Faculty of Engineering Sciences, GIK Institute of Engineering Sciences and Technology, Topi 23640, Khyber Pakhtunkhwa, Pakistan.

E-mail: kabirkhanak1@gmail.com

Abstract. The neutron capture rates and temperature dependent stellar beta decay rates of Mo isotopes are investigated within the framework of the statistical code (Talys v1.96) and proton-neutron quasi particle random phase approximation (pn-QRPA) models. The Maxwellian average cross-section (MACS) and neutron capture rates for $^{95-98}\text{Mo}(n,\gamma)^{96-99}\text{Mo}$ radiative capture processes are analyzed within the framework of statistical code Talys v1.96 based on the phenomenological nuclear level density (NLD) parameters and gamma strength functions (GSFs). The current model-based computed data for MACS provide a good comparison with the existing measured data. The temperature-dependent stellar β^- -decay rates of $^{95-98}\text{Mo}$ are investigated at different densities within the framework of the pn-QRPA model. For the considered temperature range, the neutron capture rates were found to be higher, by orders of magnitude, than the stellar β^- rates.

Keywords: Cross-section, Asymptotic Giant Branch stars, MACS, talys, nuclear level density, nuclear rates

1. Introduction

The energy production in stars [1], the associated nucleosynthesis [2, 3] and supernova explosion dynamics [4] are still not fully understood. To date, these processes have been extensively investigated by astrophysicists in an attempt to understand how our universe works. Weak-interaction mediated rates play a crucial role during the nucleosynthesis process and the evolution of the core of massive stars.

Nuclei, more massive than iron, are mostly formed by neutron capture reactions, which are called after their widely distinct time scales as the *s*-process (slow neutron capture process) and the *r*-process (rapid neutron capture process) [2, 3]. The *s*-process in the present model of stellar nucleosynthesis is more challenging than previously believed [5]. The elements from Fe to Zr ($A \leq 90$) are formed by the so-called weak component, which is driven by neutrons produced through the $^{22}\text{Ne}(\alpha, n)^{25}\text{Mg}$ reaction in massive stars. Thus, a stellar model to describe the weak *s*-process requires accurate and reliable Maxwellian average cross-section (MACS) at *s*-process relevant temperatures. The main *s*-process operates in the AGB stars and produces the heavier isotopes up to the lead-bismuth region. Because of the breakthroughs in astronomical observations and stellar modeling, accurate assessments of the *s*-process have become incredibly influential [6]. The current stellar model suggests that the neutron production for the weak *s*-process occurs in two different burning stages: the He core burning and the Carbon shell burning [7]. The burning temperatures of the two stages are not the same ($T_9 \sim 0.3$ for the He core burning and $T_9 \sim 1$ for the carbon shell burning, where T_9 is the temperature in units of 10^9 K). Hence, the *s*-process takes place when $0.3 < T_9 < 1$ and at neutron density of $N_n \approx 10^8 \text{ cm}^{-3}$ [8]. The *s*-process has evolved from a simple explanation of the abundance distribution of elements in the solar system to a more comprehensive description that takes into account the general features of stellar and galactic dynamics. As a result of such advancements, the *s*-process has become a powerful tool for examining the evolution of red giant stars [9].

Here, we focus the reader's attention towards the race between $^{95-98}\text{Mo}(n, \gamma)^{96-99}\text{Mo}$ and $^{95-99}\text{Mo} \rightarrow ^{95-99}\text{Tc} + e + \nu_e$ processes within the framework of Talys v1.96 and the pn-QRPA approach. Substantial progress has been achieved in the analysis of Mo nuclei from the astrophysical perspectives. Advances in nuclear modeling and observational techniques have allowed researchers to gain a better understanding of the nucleosynthesis of heavy elements in stars. The MACS of $^{95-98}\text{Mo}$ are crucial quantities in determining the rates. Neutron interaction cross-sections with Molybdenum play a crucial role in diverse

scientific and technological applications, from nuclear astrophysics to the operation of nuclear power plants. Mo isotopes are identified as a contaminant in pre-solar silicon carbide grains and play a critical role in the nucleosynthesis processes occurring in the AGB stars [10]. It is suggested that low uncertainty in neutron capture cross-section of Mo isotopes is highly desirable for accurate mapping of nucleosynthesis in low-mass AGB stars [11]. In the past, several authors have studied neutron capture cross-sections of Mo isotopes at different energy ranges, theoretically and experimentally [12, 13, 14, 15]. Saumi *et al.* [12] studied the MACS for the nuclei participating in the *s*-process and the *p*-process nucleosynthesis in and around the $N=50$ closed neutron shell. They have constructed a microscopic optical-model potential by the folding DDM3Y nucleon-nucleon interaction with the radial matter density of the target, obtained from relativistic mean-field (RMF). Their computed MACS at $kT=30$ keV for the $^{95-98}\text{Mo}(n, \gamma)^{96-99}\text{Mo}$ were 212 mb, 113 mb, 299 mb and 73.8 mb, respectively. Neutron capture cross-sections of seven stable isotopes of Mo have been measured using a 40 m station of the Oak Ridge Electron Linear Accelerator (ORELA) in the energy range ($3 < E_n < 90$) keV [16]. Recently, Ref. [17] measured the capture cross-section and transmission of natural Mo using an accurate neutron-nucleus reaction measurement instrument (ANNRI) situated in the material life and science facility (MLF) at J-PARC. Measurements of capture and total cross-sections for isotopes $^{94,95,96}\text{Mo}$ have been conducted at neutron time-of-flight facilities, n_TOF at CERN and GELINA at JRC-Geel, using samples with an enrichment exceeding 95% for each isotope [18]. The transmission parameters obtained in the experiment have been used to validate the resonance parameter files for Mo isotopes. Massimi *et al.* [19] measured the neutron capture cross-section in EAR1 and EAR2 at the n_TOF facility to reduce the uncertainty in the presently known data for the stable isotopes $^{94,95,96}\text{Mo}$. ^{98}Mo is the stable and most abundant isotope with an abundance of 24.13%. Understanding the thermal neutron cross-section and the resonance integral for the $^{98}\text{Mo}(n, \gamma)^{99}\text{Mo}$ reaction is crucial due to the utilization of neutron activation cross-section data in the production of ^{99}Mo and its potential applications in various studies related to neutron-matter interactions [20]. Existing literature contains numerous experimental and evaluated datasets on the thermal neutron capture cross-sections and resonance integrals for the $^{98}\text{Mo}(n, \gamma)^{99}\text{Mo}$ reaction. The authors in Ref. [21] studied the cross-section of $^{98}\text{Mo}(n, \gamma)^{99}\text{Mo}$ using monochromatic thermal neutron beam at low energies. The obtained cross-sections are 116 ± 7 mb and 91 ± 5 mb at energies 0.0334 eV and 0.0536

eV, respectively, agrees with the ENDF/B-VII data files and JENDL-4. The formation cross-section of ^{99}Mo through $^{98}\text{Mo}(n,\gamma)$ reaction is found to be 132.05 ± 32.89 mb using the activation method and off-line γ -ray spectrometric technique [22].

The suggested nuclei ($^{95-98}\text{Mo}$) in the present work are stable isotopes of Mo. Since the β decay lifetime of $^{95-99}\text{Mo}$ is temperature-sensitive, one must also take into account the fact that the production and destruction of $^{95-99}\text{Mo}$ depend on the $^{22}\text{Ne}(\alpha,n)^{25}\text{Mg}$ reaction rate (act as neutron source), which is even more temperature-sensitive. The race between $^{95-99}\text{Mo}(n,\gamma)^{96-100}\text{Mo}$ and $^{95-99}\text{Mo} \rightarrow ^{95-99}\text{Tc} + e + \nu_e$ determines the abundance of $^{95-99}\text{Mo}$ in the s -process environment. Therefore, higher temperatures do not always result in lower Mo abundances. The increase in neutron production rates from the $^{22}\text{Ne}(\alpha,n)^{25}\text{Mg}$ reaction at high temperatures more than compensates for the thermally enhanced β^- decay rate.

The present study is structured as follows: Section 2 provides a quick overview of the basic formalism. Section 3 summarizes the results of our calculations and how they compare to previous findings and measurements. Our findings are summarized in Section 4.

2. Theoretical Framework

2.1. The Talys v1.96 code

The Talys v1.96 code [23] is based on the Hauser-Feshbach theory [24, 25]. The main inputs in the Hauser-Feshbach theory are the NLDs, the optical model potentials (OMPs), and the gamma strength functions (GSFs). The effect of altering the OMPs can be disregarded in favor of the other two components when low-energy neutrons are used as incident particles (NLDs and GSFs) [26]. The optical model, employed in this study, is the local OMP by Koning and Delaroche [27]. The results were evaluated for all combinations of the phenomenological NLDs (constant temperature model (CTM), back-shifted Fermi gas model (BSFM), generalized superfluid model (GSM) [28, 29, 30, 31]) and GSFs (Kopecky-Uhl Lorentzian, Brink-Axel Lorentzian, and Gogny D1M QRPA [32, 33, 34, 35]). To describe NLD at a quantitative level, it is desired that the model is able to reproduce all experimentally known discrete levels that are available in a published database. Without this step, one may doubt the model's predictive ability for cases where no data exist. The nuclear level density (NLD) is a crucial input in statistical computations since it is employed when information about the discrete level is unavailable. The predictions of the Talys v1.96 code have been compared with the existing experimental

data. The MACS have been computed with neutron energies up to 100 keV. The abundances for the s - and the r - processes may be reproduced through the sensitivity simulations of these processes. However, one of the major sources of uncertainty lies in the correct estimation of nuclear properties such as the neutron capture cross-section and rates for the nuclei involved in these processes.

The Talys v1.96 code used for the simulation of nuclear reactions includes several state-of-the-art nuclear models to cover almost all key reaction mechanisms encountered for light particle-induced nuclear reactions. It provides an extensive range of reaction channels. The possible incident particles can be simulated in the $E_i=(0.001-200)$ MeV energy range, and the target nuclides can be from $A=12$ onwards. The output of the nuclear reaction includes fractional and total cross-sections, angular distributions, energy spectra, double-differential spectra, MACS, and capture rates. Radiative capture is important in the context of nuclear astrophysics in which a projectile fuses with the target nucleus and emits γ -ray [36, 37, 38, 39, 40]. The nuclear cross-section is an important factor in the calculation of radiative capture rates. The Maxwellian averaged cross-section is used when the energies of the projectiles follow a Maxwellian distribution, like in the stellar environment. MACS is an average of the cross-section over a range of energies, weighted by the Maxwell-Boltzmann distribution.

$$\langle\sigma\rangle(kT) = \frac{2}{\sqrt{\pi}(kT)^2} \int_0^\infty E\sigma(E)\exp\left(\frac{-E}{kT}\right)dE, \quad (1)$$

where k , is the Boltzmann constant, T is the temperature, $\sigma(E)$ is the capture cross-section and E is the projectile energy. In statistical models for predicting nuclear reactions, level densities are needed at excitation energies where discrete level information is not available or is incomplete. Together with the optical model potential, a correct level density is perhaps the most crucial ingredient for a reliable theoretical analysis of cross-sections, angular distributions, and other nuclear quantities. Six different level density models, among them three phenomenological and the rest microscopic, are included in the Talys code. For each of the phenomenological models, the constant temperature model (CTM), the back-shifted Fermi (BSFM) gas model, and the generalized superfluid model (GSM), a version without explicit collective enhancement is considered. In the CTM, the excitation energy range is divided into low energy regions i.e., from 0 keV up to the matching energy (E_M) and high energy above the E_M where the fermi-gas model (FGM) applies. Accordingly, the constant temperature part of the total

level density reads as

$$\rho_T^{tot}(E_x) = \frac{1}{T} \exp\left(\frac{E_x - E_o}{T}\right), \quad (2)$$

where T and E_o serve as adjustable parameters in the constant temperature expression. The BSFM is used for the whole energy range by treating the pairing energy as an adjustable parameter

$$\rho_F^{tot}(E_x) = \frac{1}{\sqrt{2\pi}\sigma} \frac{\sqrt{\pi} \exp(2\sqrt{aU})}{12 a^{1/4} U^{5/4}}, \quad (3)$$

where σ is the spin cut-off parameter, which represents the width of the angular momentum distribution, U is the effective excitation energy and a is the level density parameter defined below

$$a = \tilde{a} \left(1 + \delta W \frac{1 - \exp(-\gamma U)}{U}\right), \quad (4)$$

where $\tilde{a} (= \alpha A + \beta A^{2/3})$ is the asymptotic level density without any shell effects. A is the mass number, α , β and γ are global parameters that need to be determined to give the best average level density description over a whole range of nuclides. They are determined by fitting to experimental level density data. δW gives the shell correction energy, and the damping parameter γ determines how rapidly a approaches to \tilde{a} . One should note that for the best fitting, a can be readjusted to achieve the desired value of cross-section and nuclear reaction rates. For further investigations, one can refer to [41]. The GSM is similar to CTM in the way that it also divides the energy range into low and high energies. The high energy range is described by BSFM as mentioned before. It is characterized by a phase transition from a superfluid behavior at low energies, where the pairing correlations strongly influence the level density.

$$\rho^{tot}(E_x) = \frac{1}{\sqrt{2\pi}\sigma} \frac{e^S}{\sqrt{D}}, \quad (5)$$

where S is the entropy and D is the determinant related to the saddle-point approximation. The gamma strength function (GSF) plays a crucial role in estimating cross-sections and reaction rates, particularly in processes involving the emission of gamma rays. Different GSFs are included in Talys v1.96, among them the Brink-Axel model is used for all transitions except for $E1$ [23]. The GSF function f_{XL} gives the distribution of the average reduced partial transition width as a function of the photon energy E_γ .

$$f_{XL}(E_\gamma) = K_{XL} \frac{\sigma_{XL} E_\gamma \Gamma_{XL}^2}{(E_\gamma^2 - E_{XL}^2)^2 + (E_\gamma \Gamma_{XL}^2)^2}, \quad (6)$$

where E_{XL} is the energy, Γ_{XL} is the width, and σ_{XL} is the giant resonance strength. For $E1$ transitions, Talys v1.96 utilizes the Kopecky-Uhl model by default.

$$f_{XL}(E_\gamma, T) = K_{XL} \left[\frac{E_\gamma \tilde{\Gamma}_{E1}(E_\gamma)}{(E_\gamma^2 - E_{E1}^2)^2 + E_\gamma^2 \tilde{\Gamma}_{E1}(E_\gamma)^2} + \frac{0.7 \Gamma_{E1} 4\pi^2 T^2}{E_{E1}^3} \right] \sigma_{E1} \Gamma_{E1} \quad (7)$$

and

$$\tilde{\Gamma}_{E1}(E_\gamma) = \Gamma_{E1} \frac{E_\gamma^2 + 4\pi^2}{E_{E1}^2} \left[\frac{E_n + S_n - \Delta - E_\gamma}{a(S_n)} \right], \quad (8)$$

where $\tilde{\Gamma}(E_\gamma)$ represents the energy-dependent damping width, E_n is the incident energy of neutrons, S_n is the neutron separation energy, and Δ is the correction for pairing. a represents the level density parameter at S_n as mentioned earlier.

2.2. The pn-QRPA model

The stellar β^- decay rates are investigated within the framework of pn-QRPA. The Hamiltonian of the model is presented as

$$H^{QRPA} = H^{sp} + V^{pair} + V_{GT}^{ph} + V_{GT}^{pp}. \quad (9)$$

The deformed Nilsson potential (H^{sp}) basis was utilized to compute wave functions and single particle energies. V^{pair} pairing forces were treated employing the BCS formalism. Q-values and residual interactions have a considerable influence on the computed electron emission (β^-) rates and associated half-lives [42]. The V_{GT}^{ph} (χ (ph)), V_{GT}^{pp} (κ (pp)) known as the residual interactions, were taken into account for the calculation of GT strength. For a thorough definition of χ and κ , as well as the optimal choice of these parameters, see into Refs. [42, 43, 44, 45].

The V_{GT}^{ph} force was found employing

$$V_{GT}^{ph} = +2\chi \sum_{\mu=-1}^1 (-1)^\mu Y_\mu Y_{-\mu}^\dagger, \quad (10)$$

with

$$Y_\mu = \sum_{j_p m_p j_n m_n} \langle j_p m_p | t_- \sigma_\mu | j_n m_n \rangle c_{j_p m_p}^\dagger c_{j_n m_n}. \quad (11)$$

Whereas the V_{GT}^{pp} interaction was determined employing

$$V_{GT}^{pp} = -2\kappa \sum_{\mu=-1}^1 (-1)^\mu P_\mu^\dagger P_{-\mu}, \quad (12)$$

with

$$P_\mu^\dagger = \sum_{j_p m_p j_n m_n} \langle j_n m_n | (t_- \sigma_\mu)^\dagger | j_p m_p \rangle \times (-1)^{l_n + j_n - m_n} c_{j_p m_p}^\dagger c_{j_n - m_n}^\dagger, \quad (13)$$

where the operators are explained below and the other symbols have their normal meanings. The χ and κ were taken from Ref. [45]. Reduced GT transition probabilities were achieved by expressing the QRPA ground state into one-phonon states in the daughter nucleus. Additional input variables for the calculation of weak transitions include the pairing gap (Δ_p , Δ_n), nuclear deformation (β_2), threshold-values of energy and Nilsson potential variables (NPV). We adjusted our computation with nuclear deformation parameters from the most current analysis [46]. The NPV were taken from [47], and the oscillator constant (which is similar for proton and neutron) was identified using the equation $\hbar\omega = 41A^{-1/3}$ (in MeV). We employed the Nilsson potential to calculate the wave function. The Nilsson framework is often used to characterize the framework of low-lying states. We used the β_2 as a Nilsson potential input variable. Primarily, wave functions and single particle energies were calculated on the deformed Nilsson basis. The transformation from the spherical nucleon basis (c_{jm}^+ , c_{jm}) to the axial symmetric deformed basis ($d_{m\alpha}^+$, $d_{m\alpha}$) were performed

$$d_{m\alpha}^+ = \sum_j D_j^{m\alpha} c_{jm}^+. \quad (14)$$

The $D_j^{m\alpha}$ is a group of Nilsson eigenfunctions with α as an additional quantum number to characterize the Nilsson eigen-states. The BCS formalism was used in the Nilsson basis for neutron/proton system separately. The diagonalization of the Nilsson Hamiltonian yielded the transformation matrices (a detailed explanation may be found in [44, 48]). The globally systematic pairing gap values, $\Delta_n = \Delta_p = 12/\sqrt{A}$ (MeV), were employed in our computation. The Q-values were obtained from the most current assessment of atomic mass data by [49]. Further details of solution of Eq. (9) may be studied from [50]. One may view the computation of terrestrial β^- half-lives in Ref. [43]. Further information on the formalism utilized to estimate GT transitions in stellar scenarios using the pn-QRPA technique can be found in Refs. [51, 52].

The electron emission rates/positron capture (pc) rates ($\lambda_{ij}^{(\beta^-/pc)}$) from the parent nucleus (i th-state) to the daughter nucleus (j th-state) is given by

$$\lambda_{ij}^{(\beta^-/pc)} = \ln 2 \frac{f_{ij}(T, \rho, E_f)}{(ft)_{ij}}, \quad (15)$$

where $(ft)_{ij}$ is related to the reduced transition probability (B_{ij}) by the relation

$$(ft)_{ij} = D/B_{ij}. \quad (16)$$

The value of D is taken as 6143 s [53], and B_{ij} is defined below

$$B_{ij} = B(F)_{ij} + (g_A/g_V)^2 B(GT)_{ij}, \quad (17)$$

where $B(F)$ and $B(GT)$ are reduced transition probabilities of the Fermi and Gamow Teller transitions, respectively. f_{ij} are the phase space integrals. Further details can be found in Ref. [52]. Because of the high temperatures in the stellar core, β^- and pc rates get only a minor contribution from parent excited energy levels. We utilize the Boltzmann distribution function to compute the occupancy probability of the parent i th-state

$$P_i = \frac{\exp(-E_i/kT)}{\sum_{i=1} \exp(-E_i/kT)}. \quad (18)$$

Furthermore, the total stellar β^-/pc rates were computed using

$$\lambda^{(\beta^-/pc)} = \sum_{ij} P_i \lambda_{ij}^{(\beta^-/pc)}. \quad (19)$$

The summation stands for computation of all parent and daughter energy levels until satisfactory convergence is achieved. We noticed that in our present work of weak β^- and pc calculations, a large model space (up to 7 $\hbar\omega$ major oscillatory shells) makes it easier to achieve the desired convergence. The ability to calculate the weak rates of any heavy nuclear species is one of the main advantages of the pn-QRPA technique with the chosen Hamiltonian (Eq. (9)).

2.3. The stellar neutron capture rates ($\lambda_{(n,\gamma)}$)

The total neutron capture rate ($\lambda_{(n,\gamma)}$ in the units of s^{-1}) is defined as [54]

$$\lambda_{(n,\gamma)} = v_i \times \sigma_i \times n_n, \quad (20)$$

where v_i is the averaged velocity of neutron, σ_i is the MACS, and n_n is the average neutron density for $T_9 < 1$

$$n_n = \frac{4.3 \times 10^{36} \rho X_4 e^{[-(0.197/T_9)^{4.82}]} (\frac{1}{T_9})^{2/3} e^{\frac{-47}{(T_9)^{1/3}}}}{\sigma_{22} [1 + \sigma_i N_i / \Sigma \sigma_{22} N_{22}] (\frac{T_9}{0.348})^{1/2}}, \quad (21)$$

where X_4 is the helium mass fraction, ρ is the nuclear matter density and T_9 is the temperature at the base of the convective shell. σ_{22} is the $^{22}\text{Ne}(n, \gamma)^{23}\text{Ne}$ capture cross-section. N_i is the abundance of species i and σ_i is their MACS. The composition of heavy nuclei at the base of the convective shell is dominated by ^{22}Ne produced by α - captures on ^{14}N from the CNO cycle.

3. Results and Discussion

For some applications, such as astrophysical investigations involving nuclei along neutron or proton drip lines, it is crucial to extrapolate the data much beyond the experimentally known region. Large scale

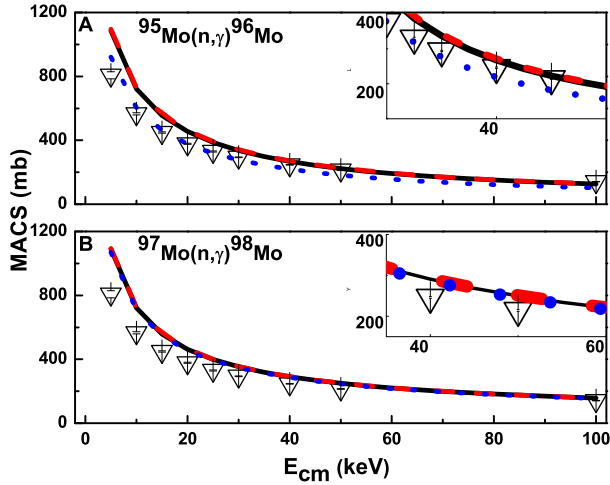


Figure 1: The total MACS for $^{95,97}\text{Mo}(n,\gamma)^{96,98}\text{Mo}$ along with the measured data (∇) [55]. (A) The computed MACS for the $^{95}\text{Mo}(n,\gamma)^{96}\text{Mo}$ by the BSFM with the GSFs as Brink-Axel (solid line), Gogny (dashed line) and Kopecky-Uhl (dotted line). (B) The computed MACS for the $^{97}\text{Mo}(n,\gamma)^{98}\text{Mo}$ by the BSFM with the GSFs as Brink-Axel (solid line), Gogny (dashed line) and Kopecky-Uhl (dotted line).

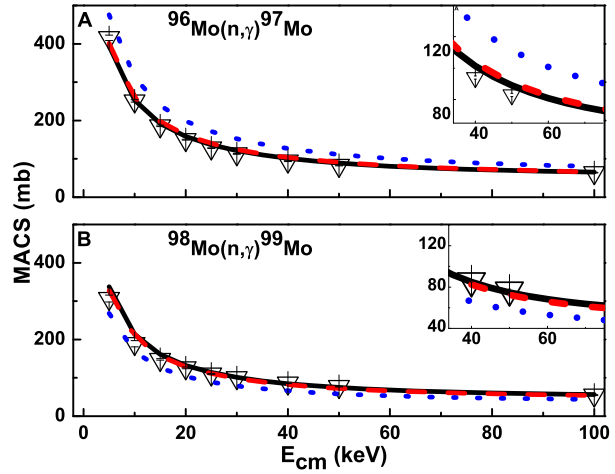


Figure 2: The total MACS for $^{96,98}\text{Mo}(n,\gamma)^{97,99}\text{Mo}$ along with the measured data (∇) [55]. (A) The computed MACS for the $^{96}\text{Mo}(n,\gamma)^{97}\text{Mo}$ by the BSFM with the GSFs as Brink-Axel (solid line), Gogny (dashed line) and Kopecky-Uhl (dotted line). (B) The computed MACS for the $^{98}\text{Mo}(n,\gamma)^{99}\text{Mo}$ by the BSFM with the GSFs as Brink-Axel (solid line), Gogny (dashed line) and Kopecky-Uhl (dotted line).

applications thus need to use data from reliable theoretical models. Inaccurate NLD description or prediction is the main source of uncertainty in statistical model predictions. Since experiments are not attainable at all energies, it is evident that theoretical extrapolations are critical. Here, we have used the nuclear level density model and a variety γ -strength functions to compute the MACS for $^{95-98}\text{Mo}$ isotopes. The present-listed Mo isotopes are almost β stable in terrestrial environments. We have investigated the MACS $^{95-98}\text{Mo}(n,\gamma)^{96-99}\text{Mo}$ for a range of temperatures appropriate for the presumed site of the s -process of nucleosynthesis. The considered isotopes under investigations have almost magic neutron configurations, which results in their small (n,γ) cross-sections and fairly large s -abundances. The MACS $^{95-98}\text{Mo}(n,\gamma)^{96-99}\text{Mo}$ are computed via Talys v1.96 in the Hauser-Feshbach framework by choosing the NLDs, and a radiative strength function. Out of several possibilities for level density calculations, we employed the phenomenological NLDs as BSFM for excitation energies up to 100 keV. The obtained NLDs computed by the BSFM were employed for the calculation of MACS for $^{95-97}\text{Mo}(n,\gamma)^{96-98}\text{Mo}$. One should note that we employed NLD as BSFM and varied the GSFs. For example, we have fixed the NLD as a BSFM and varied the GSFs as Brink-Axel, Gogny, and Kopecky-Uhl. Together with the findings of Ref. [55], the Maxwellian

average cross-section results for $^{95,97}\text{Mo}(n,\gamma)$ within $(0.01 < kT < 100 \text{ keV})$ are shown in Figs. (1)A,B. The computed results based on the present model agree well with the data of Ref. [55], both above and below the s -process energy $kT=30 \text{ keV}$. Note that in order to get the best-fitting with the measured data, we adjusted the parameter a as mentioned in Eq. (4). In the present case, the adjustment parameter a were obtained 0.5 through adjustment to all available experimental of the MACS. Similarly, $^{96,98}\text{Mo}(n,\gamma)^{97,99}\text{Mo}$ radiative capture processes were analyzed using the NLD as a BSFM and the same sets of GSFs (as previously mentioned). Fixing the NLD as BSFM and changing the GSFs as Gogny, Kopecky-Uhl, and Brink-Axel. The energy dependence Maxwellian averaged cross-sections for ^{96}Mo and ^{98}Mo isotopes are depicted in Figs. (2)A,B along with the results of Ref. [55]. The computed MACS at $kT=30 \text{ keV}$ in the analysis of $^{96}\text{Mo}(n,\gamma)^{97}\text{Mo}$ were 121.35 mb (GSF as Brink-Axel), 124.31 mb (GSF as Gogny), and 152.29 mb (GSF as Kopecky-Uhl). It is observed that the current model-based results agree well with the 113 mb MACS at $kT=30 \text{ keV}$ found in Ref. [55]. Similarly, the computed MACS at $kT=30 \text{ keV}$ for the analysis of $^{98}\text{Mo}(n,\gamma)^{99}\text{Mo}$ were 101.28 mb (GSF as Brink-Axel), 98.42 mb (GSF as Gogny), and 78.80 mb (GSF as Kopecky-Uhl). Remarkably, at $kT=30 \text{ keV}$, the current model-based results agree well with the MACS reported in Ref. [55].

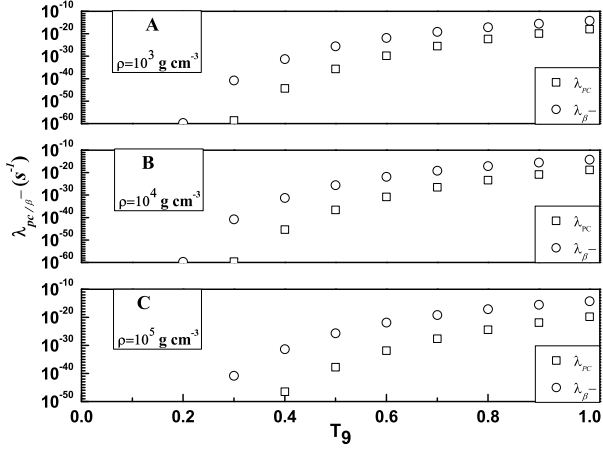


Figure 3: The λ_{pc} and λ_{β^-} rates for the β decay of ^{95}Mo .

Stellar β rates of $^{95-98}\text{Mo}$ nuclei have been analyzed using the pn-QRPA model in the second part of our study. The pn-QRPA Hamiltonian defined by Eq. (9) has Nilsson deformed potential and residual interaction terms. In the present study, we used the nuclear deformation (β_2) from the Finite Range Droplet Model (FRDM) model as an input parameter in our pn-QRPA model for the selected Mo isotopes. The nuclear β_2 value was used in our computation as a free parameter. The β_2 values from the most recent

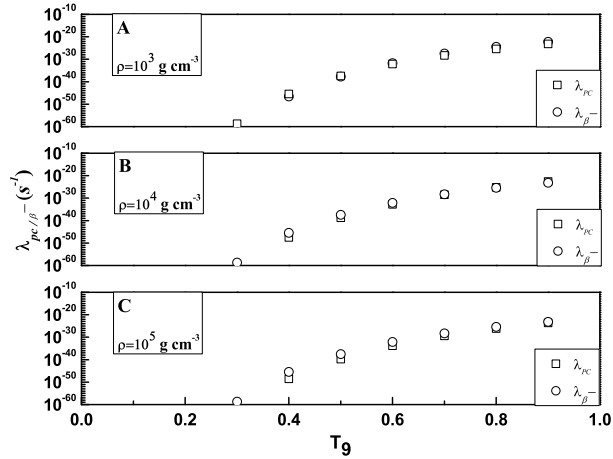


Figure 4: The λ_{pc} and λ_{β^-} rates for the β decay of ^{96}Mo .

globally updated FRDM [46] computation served as the foundation for our calculations. The β_2 values are 0.000 (^{95}Mo), 0.150 (^{96}Mo), 0.172 (^{97}Mo) and 0.206 (^{98}Mo). The residual interactions χ and κ values in the present cases are optimized based on Ref. [45] and satisfied the Ikeda sum rule. Based on the optimized values of the residual interactions, we have computed

the stellar β^- decay and pc rates. The results of our present investigations are depicted in Figs. (3-6)A-C at densities $\rho=10^3-10^5 \text{ g cm}^{-3}$. Even though these Mo

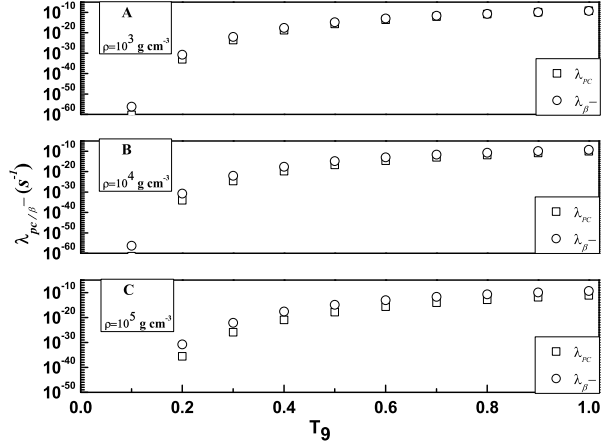


Figure 5: The λ_{pc} and λ_{β^-} rates for the β decay of ^{97}Mo .

isotopes are stable in terrestrial environments, they have higher β^- decay than pc rates at lower and even higher temperatures. At low density $\rho=10^3 \text{ g cm}^{-3}$, and lower temperatures, the λ_{β^-} are higher than the λ_{pc} ; however, at high temperatures, the λ_{pc} increases gradually because more positrons are created at high temperatures. For ^{95}Mo there is a clear difference between the λ_{pc} and λ_{β^-} at higher densities, as mentioned in Fig. (3)A-C. Similarly, Fig. (4-6)A-C

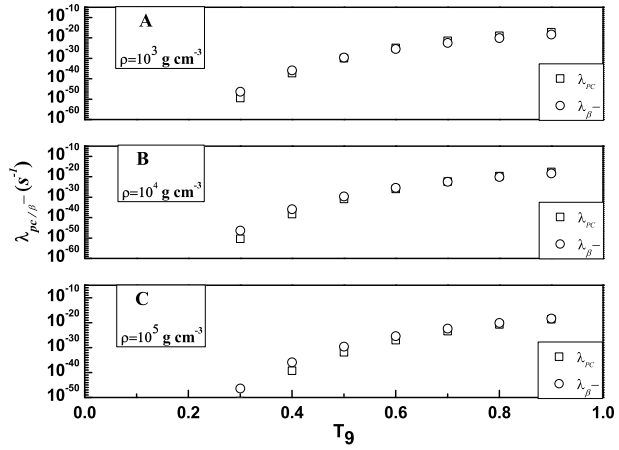


Figure 6: The λ_{pc} , and λ_{β^-} rates, at all densities, for the β decay of ^{98}Mo .

display the λ_{pc} and λ_{β^-} rates for $^{96}\text{Mo}-^{98}\text{Mo}$ nuclei at $\rho=(10^3-10^5) \text{ g cm}^{-3}$. We noted that the stellar β^- decay rates increase with temperature, but in the heavier nuclei of Mo, the λ_{pc} and λ_{β^-} are almost the same at higher temperatures.

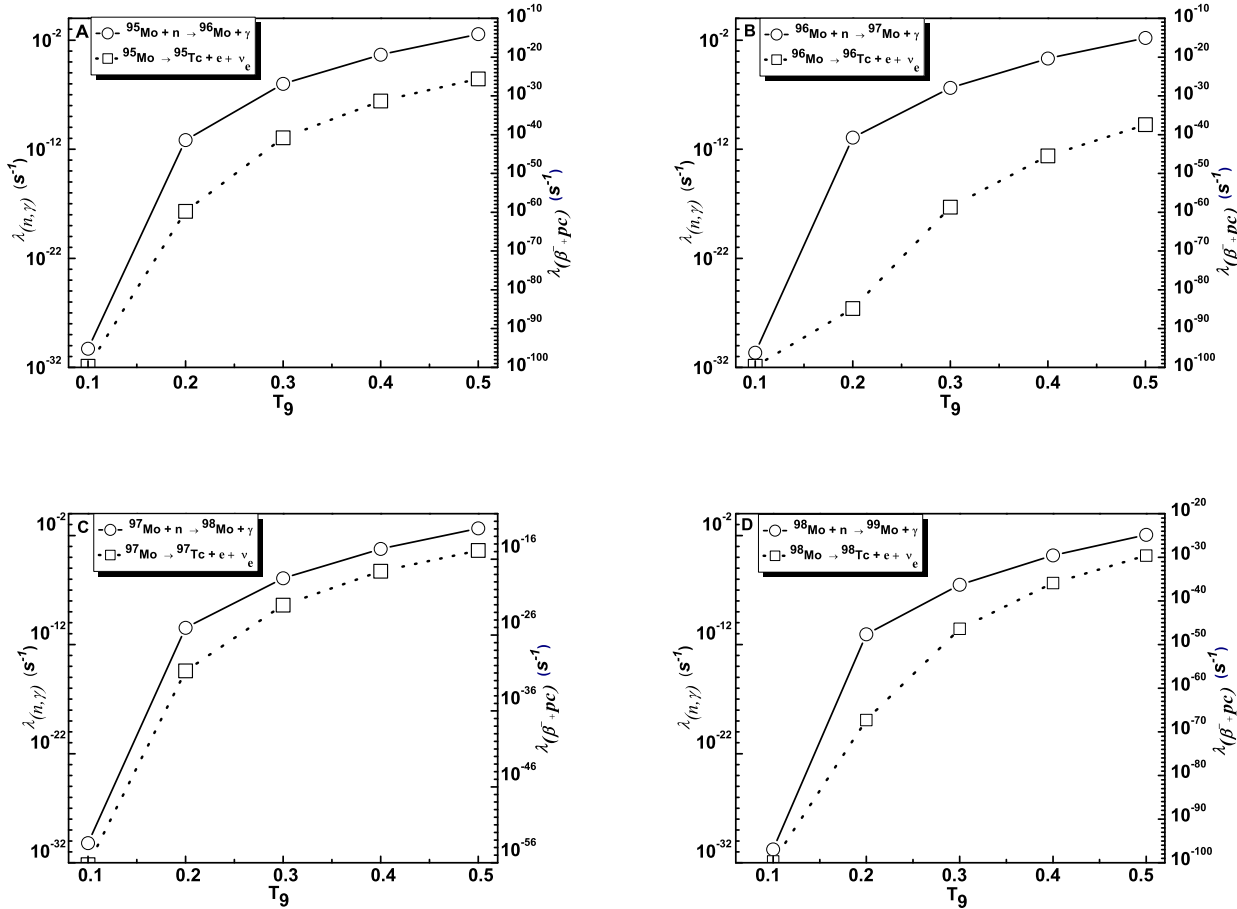


Figure 7: Neutron capture rates ($\lambda_{(n,\gamma)}$) and stellar β decay rates ($\lambda_{(\beta+pc)}$) of $^{95-98}\text{Mo}$ nuclei at $\rho=10^4 \text{ g cm}^{-3}$. (A). The computed $\lambda_{(n,\gamma)}$ and $\lambda_{(\beta+pc)}$ for ^{95}Mo . (B). The computed $\lambda_{(n,\gamma)}$ and $\lambda_{(\beta+pc)}$ for ^{96}Mo . (C). The computed $\lambda_{(n,\gamma)}$ and $\lambda_{(\beta+pc)}$ for ^{97}Mo . (D). The computed $\lambda_{(n,\gamma)}$ and $\lambda_{(\beta+pc)}$ for ^{98}Mo .

As part of the third phase of this investigation, we have calculated the sum of stellar β^- decay and pc rates ($\lambda_{(\beta+pc)}$) and the temperature-dependent neutron capture rates ($\lambda_{(n,\gamma)}$) for the selected Mo isotopes. For the calculations of $\lambda_{(n,\gamma)}$, we employed Eq. (20). In the initial set of computations, we identified the best-fitting model combination for each isotope, which in our investigation is Brink-Axel as a GSF and BSFM as an NLD. Based on the relevant MACS, we have computed the $\lambda_{(n,\gamma)}$. The present computed MACS for ^{95}Mo (276 mb at $E_n=30$ keV) and for ^{97}Mo (347 mb at $E_n=30$ keV). With these cross-sections, the total neutron capture rate for ^{95}Mo and ^{97}Mo are $\lambda_{(n,\gamma)}=6.60\times 10^{-17}n_n$ and $\lambda_{(n,\gamma)}=8.305\times 10^{-17}n_n$, respectively. Similarly, with neutron capture cross-sections for ^{96}Mo (121 mb at $E_n=30$ keV) and for ^{98}Mo (98 mb at $E_n=30$ keV), the total capture rates for ^{96}Mo and ^{98}Mo are $\lambda_{(n,\gamma)}=2.90\times 10^{-17}n_n$ and $\lambda_{(n,\gamma)}=2.34\times 10^{-17}n_n$, respectively. At $\rho=10^4 \text{ g cm}^{-3}$ and $X_4=0.2$ the present computed $\lambda_{(n,\gamma)}$ and $\lambda_{(\beta+pc)}$ are depicted in Fig. (7)A-D for the

$^{95-98}\text{Mo} + n \rightarrow ^{96-99}\text{Mo} + \gamma$ and $^{95-98}\text{Mo} \rightarrow ^{95-98}\text{Tc} + e + \nu_e$. It is obvious that, at lower temperature the thermally enhanced β decay rates are much lower in magnitude than $\lambda_{(n,\gamma)}$. For example, at $T_9=0.1$, $\lambda_{(n,\gamma)}=5.1\times 10^{-31} \text{ s}^{-1}$ while at the same temperature, $\lambda_{(\beta+pc)}$ is $0.97\times 10^{-100} \text{ s}^{-1}$ for ^{95}Mo . At higher temperature $T_9=0.5$, $\lambda_{(n,\gamma)}=3.5\times 10^{-02} \text{ s}^{-1}$ and $\lambda_{(\beta+pc)}$ is $2.37\times 10^{-26} \text{ s}^{-1}$. For ^{97}Mo , at $T_9=0.1$, $\lambda_{(n,\gamma)}=6.4\times 10^{-31} \text{ s}^{-1}$ while at the same temperature $\lambda_{(\beta+pc)}$ is $5.5\times 10^{-56} \text{ s}^{-1}$. But at $T_9=0.5$ $\lambda_{(n,\gamma)}=4.4\times 10^{-02} \text{ s}^{-1}$ and $\lambda_{(\beta+pc)}$ is $1.37\times 10^{-15} \text{ s}^{-1}$. Therefore, in the examined physical conditions, the neutron capture rates of Mo isotopes exceed the thermally enhanced beta decay rates both at lower and higher temperatures.

4. Conclusion

Below we present a summary of our main findings and make some inferences.

1. We have examined the MACSs of the (n,γ) process

for the sets of β stable Mo nuclei with magic or almost magic neutron numbers in the context of the Talys v1.96 code across a broad energy range. We deduced lower capture cross-section for $^{96,98}\text{Mo}(n,\gamma)^{97,99}\text{Mo}$ than $^{95,97}\text{Mo}(n,\gamma)^{96,98}\text{Mo}$, usually included in models of the s -process in AGB stars. It should be noted that Talys provides a data representation of the phenomenological sets of NLDs and GSFs that are relatively similar. Several NLD and GSF models from Talys have been used to generate the MACS for the $^{95-98}\text{Mo}(n,\gamma)^{96-99}\text{Mo}$ processes. Following that, the generated values were contrasted with the measurements found in the literature. We found that, out of all the GSF models, the Brink-Axel of Talys is the best fit for the $^{95-98}\text{Mo}(n,\gamma)^{96-99}\text{Mo}$ processes. For these nuclei, the Hauser-Feshbach theory prediction accurately reproduces the available experimental data with all parameter modifications and model variations.

2. We computed the β^-/pc rates based on the pn-QRPA framework for different densities and temperatures. The pn-QRPA theory effectively calculates weak interaction rates for $^{96-98}\text{Mo}$. Our analysis included a broad model space of $7\hbar\omega$. Weak rates for a wide range of stellar temperatures and densities were calculated. We noted that the weak rates increase directly with temperature. This is due to the fact that at higher temperatures, the occupation probability of parent excited states increase and partial rates from parent excited levels have a finite contribution to the total rate (Eq. (19)).

3. We compared $\lambda_{(n,\gamma)}$ and $\lambda_{(\beta^+pc)}$ under an appropriate stellar scenario in the third phase of our investigations. It was noted that the stellar β -decay rates are much lower than the neutron capture rates at low temperatures. At higher temperatures, the stellar β decay increases but still are much smaller than the $\lambda_{(n,\gamma)}$ rates. For example, at $T_9=0.5$, the $\lambda_{(n,\gamma)}/\lambda_{(\beta^+pc)}=1.50\times 10^{24}$, 4.27×10^{35} , 3.22×10^{13} and 4.48×10^{27} for $^{95-98}\text{Mo}$, respectively.

From the present study, we concluded that the $\lambda_{(n,\gamma)}$ are higher than $\lambda_{(\beta^+pc)}$ rates.

5. References

- [1] H. A. Bethe, Phys. Rev. **55**, 434 (1939)
- [2] E. M. Burbidge, G. R. Burbidge, W. A. Fowler, and F. Hoyle, Rev. Mod. Phys. **29**, 547 (1957)
- [3] A. G. W. Cameron, PASP **69**, 201 (1957)
- [4] W. Baade, F. Zwicky, Proc. Natl. Acad. Sci **20**, 254 (1934)
- [5] F. Kappeler, R. Gallino, S. Bisterzo, and W. Aoki Rev. Mod. Phys **83**, 157 (2011)
- [6] M. Lugaro *et al.*, Astrophys. J **586**, 1305 (2003)
- [7] C. M. Raiteri, M. Busso, R. Gallino, and G. Picchio, Astrophys. J **371**, 665 (1991)
- [8] F. Kappeler, R. Gallino, M. Busso, G. Picchio, C. M. Raiteri, Astrophys. J **354**, 630 (1990)
- [9] M. Busso, R. Gallino, L. D. Lambert, C. Travaglio, and V. V. Smith, Astrophys. J **557**, 802 (2001)
- [10] N. Liu *et al.*, Astrophysical J **881(1)**, 28 (2019)
- [11] G. Cescutti *et al.*, MON NOT R ASTRON SOC **478(3)**, 4101 (2018)
- [12] Saumi Dutta *et al.*, Phys. Rev. C. **94**, 024604 (2016)
- [13] H. Pomerance, Phys. Rev. **88(2)**, 412 (1952)
- [14] S. V. Kapchigashev, Y. P. Popov, Soviet Atomic Energy **15(2)**, 808 (1964)
- [15] C. D. Stuepegia *et al.*, J. Nucl. Energy **22(5)**, 267 (1968)
- [16] A. D. Musgrove *et al.*, Nucl. Phys. A. **270(1)**, 108 (1976)
- [17] I. Duhamel *et al.*, In EPJ Web of Conferences **247**, 09007 92021
- [18] R. Mucciola *et al.*, In EPJ Web of Conferences **284** (2023)
- [19] C. Massimi, Measurement of $^{94,95,96}\text{Mo}(n,\gamma)$ relevant to Astrophysics and Nuclear Technology (No. CERN-INTC-2020-052) (2020)
- [20] Nguyen Van Do *et al.*, Nucl. Instrum. Methods Phys. Res. B **267**, 462 (2009)
- [21] M. S. Uddin *et al.*, Radiochim. Acta. **103(2)**, 85 (2015)
- [22] S. Badwar *et al.*, Appl. Radiat. Isot. **129**, 117 (2017)
- [23] A. J. Koning, S. Hilaire, S. Goriely TALYS-1.96 A Nuclear Reaction Program, User Manual, Nuclear Research and Consultancy Group (NRG), Netherlands. <http://www.talys.eu>. (2021)
- [24] W. Hauser, H. Feshbach, Phys. Rev **87**, 366 (1952)
- [25] S. Goriely, S. Hilaire, A. J. Koning A & A **487**, 767 (2008)
- [26] D. Rochman, S. Goriely, A. J. Koning, H. Ferroukhi, Phys Lett. B **764**, 109 (2017)
- [27] A. J. Koning, J. P. Delaroche. Nucl. Phys. A. **713**, 231 (2003)
- [28] A. Gilbert and A. G. W. Cameron Can. J. Phys. **43**, 1446 (1965)
- [29] W. Dilg *et al.*, Nucl. Phys. A **217**, 269 (1973)
- [30] A. V. Ignatyuk, K. K. Istekov, and G. N. Smirenkin, Sov. J. Nucl. Phys. **29**, 450 (1979)
- [31] A. V. Ignatyuk *et al.*, Phys. Rev. C. **47**, 1504 (1993)
- [32] D. M. Brink, Nucl. Phys. **4**, 215 (1957)
- [33] P. Axel Phys. Rev. **126**, 671 (1962)
- [34] J. Kopecky and M. Uhl., Phys. Rev. C. **41**, 1941 (1990)
- [35] S. Goriely *et al.*, Phys. Rev. C. **98**, 014327 (2018)
- [36] A. Kabir and Jameel-Un Nabi Nucl. Phys. A. **1007**, 122118 (2021)
- [37] A. Kabir *et al.*, Commun. Theor. Phys **74**, 025301 (2022)
- [38] B. F. Irgaziev *et al.*, Astrophys. Space Sci **7**, 363 (2018)
- [39] A. Kabir *et al.*, Astrophys. Space Sci **365**, 1 (2020)
- [40] A. Kabir *et al.*, J. Phys. G: Nucl. Part. Phys **49**, 075101 (2022)
- [41] A. J. Koning, S. Hilaire, S. Goriely Nucl. Phys. A. **810**, 13 (2008)
- [42] J. Engel *et al.*, Phys. Rev. C. **60**, 014302 (2015)
- [43] A. Staudt *et al.*, At. Data Nucl. Data Tables **44**, 79 (1990)
- [44] M. Hirsch *et al.*, At. Data Nucl. Data Tables **53**, 165 (1993)
- [45] H. Homma *et al.*, Phys. Rev. C. **54**, 2972 (1996)
- [46] P. Möller, *et al.*, Atom. Data Nucl. Data Tables **1090**, 1 (2016)

- [47] I. Ragnarsson, R. K. Sheline, *Phys. Ser.* **29**, 385 (1984)
- [48] K. Muto *et al.*, *Z. Phys. A.* **333**, 125 (1989)
- [49] G. Audi *et al.*, *Chin. Phys. C.* **41**, 030001 (2017)
- [50] K. Muto *et al.*, *Z. Phys. A* **341**, 407 (1992)
- [51] J.-U. Nabi, H. V. Klapdor-Kleingrothaus, *At. Data Nucl. Data Tables* **71**, 149 (1999)
- [52] J.-U. Nabi, H.V. Klapdor-Kleingrothaus, *At. Data Nucl. Data Tables* **88**, 237 (2004)
- [53] J. C. Hardy, I. S. Towner, *Phys. Rev. C.* **79**, 055502 (2009)
- [54] G. J. Mathews *et al.*, *Astrophys. J.* **302**, 410 (1986)
- [55] R. R. Winters and R. L. Macklin *Astrophysical. J* **313**, 808 (1987)

